

Article

A Novel Deformation Extraction Approach for Sub-Band InSAR and Its Application in Large-Scale Surface Mining Subsidence Monitoring

Xinpeng Diao ^{1,2,*}, Quanshuai Sun ², Jing Yang ³, Kan Wu ^{1,2} and Xin Lu ⁴¹ Jiangsu Key Laboratory of Resources and Environmental Information Engineering, Xuzhou 221116, China² School of Environment Science and Spatial Informatics, China University of Mining and Technology, Xuzhou 221116, China³ Geophysical and Geochemical Exploration Institute of Ningxia Hui Autonomous Region, Yinchuan 750021, China⁴ Gucheng Coal Mine, Lu'an Chemical Group Co., Ltd., Changzhi 046000, China

* Correspondence: xpdiao@cumt.edu.cn; Tel.: +86-15862302383

Abstract: Differential synthetic aperture radar interferometry (InSAR) is widely used to monitor ground surface deformation due to its wide coverage and high accuracy. However, the large-scale and rapid deformation that occurs in mining areas often leads to densely spaced interference fringes, thus, severely limiting the applicability of D-InSAR in mining subsidence monitoring. Sub-band InSAR can reduce phase gradients in interferograms by increasing the simulated wavelength, thereby characterising large-scale surface deformations. Nonetheless, accurate registration between non-overlapping sub-band images with conventional sub-band InSAR is challenging. Therefore, our study proposed a new sub-band InSAR deformation extraction method, based on raw full-bandwidth single-look complex image pair registration data to facilitate sub-band interferometric processing. Simulations under noiseless conditions demonstrated that the maximum difference between the sub-band InSAR-monitored results and real surface deformations was 26 mm (1.86% of maximum vertical deformation), which theoretically meets the requirements for mining subsidence monitoring. However, when modelling dynamic deformation with noise, the sub-band InSAR-simulated wavelength could not be optimised for surface deformation due to the limitation in current SAR satellite bandwidths, which resulted in significantly noisy and undistinguishable interference fringes. Nonetheless, this method could still be advantageous in high-coherence regions where surface deformation exceeds 1/5th of the simulated wavelength.

Keywords: mining subsidence; sub-band InSAR; simulation analysis; dynamic deformation

Citation: Diao, X.; Sun, Q.; Yang, J.; Wu, K.; Lu, X. A Novel Deformation Extraction Approach for Sub-Band InSAR and Its Application in Large-Scale Surface Mining Subsidence Monitoring. *Sustainability* **2023**, *15*, 354. <https://doi.org/10.3390/su15010354>

Academic Editor: Peixian Li

Received: 13 November 2022

Revised: 19 December 2022

Accepted: 21 December 2022

Published: 26 December 2022



Copyright: © 2022 by the authors. Licensee MDPI, Basel, Switzerland. This article is an open access article distributed under the terms and conditions of the Creative Commons Attribution (CC BY) license (<https://creativecommons.org/licenses/by/4.0/>).

1. Introduction

In recent years, renewable energy accounts for an increasing proportion of gross final energy consumption [1]. Although many countries and organizations have established the targets of the quick phase-out of coal in the electricity production and the increasing investments in renewables [2], the current coal output is still very large. The Statistical Review of World Energy 2022, launched by British Petroleum, stated that the world's total coal production was 8.17 billion tons, and the share of coal in the power sector increased slightly from 35% to 36% in 2021 [3]. China's sustained and rapid socio-economic development also has led to increased energy consumption, and the country's average raw coal output has reached 3.56 billion tons over the past decade. Coal mining contributes significantly to the economy; however, it also causes a series of ecological and social problems, such as ground surface subsidence, soil erosion, induced landslides, collapses, other geological disasters, and village relocation or immigration [4,5]. Coal is also the key contributor for large CO₂ emission, resulting in anthropogenic climate change [IPCC]. The root of these disasters is the

surface subsidence caused by mining, which has been one of the main reasons for destroying the ecological environment of the mining area at present, and is extremely detrimental to the harmonious and stable development of economy and society.

The real-time monitoring of the spatial distribution and temporal evolution of surface deformation caused by underground coal mining is particularly important to ensure both the safe operation of mines and safeguard human well-being and property. Traditional levelling surveys, GPS measurements, and 3D laser scanning technology provide reliable and high-accuracy observational data and, thus, play important roles in subsidence monitoring. However, these techniques are not well-suited for large-area subsidence observations due to their labour-intensive nature, high costs, low spatial coverage, and inability to accurately distinguish subsidence ranges [6]. Satellite radar remote sensing has enabled large-area monitoring of ground surface deformation. In particular, the detection accuracy of differential synthetic aperture radar interferometry (D-InSAR) can reach the centimetre or even sub-centimetre level [7]. Therefore, this technology has been widely used in deformation monitoring (e.g., coseismic displacement caused by earthquakes [8–10], crustal displacement caused by volcanic activity [11,12], single- or multiple-building deformation caused by landslides/subsidence [13–15], glacier deformation [16–18], and surface subsidence induced by underground coal mining [19,20]). Nonetheless, the results of conventional D-InSAR technology are affected by differential phase gradients and the large-scale and rapid deformation that occurs in mining areas. These conditions often lead to densely spaced interference fringes [21], which severely limit the applicability of this technology in mining subsidence monitoring.

Many experimental studies have been carried out to address the challenges of employing conventional D-InSAR to accurately and comprehensively obtain surface deformation due to excessive subsidence. Among the notable developments, time-series InSAR technologies (such as persistent scatterer InSAR and small baseline subset InSAR) can improve the magnitude and accuracy of deformation monitoring by performing high-pass and low-pass filtering in the time and spatial domains, respectively, which is considered to be the most successful approach. For example, research has been conducted on the application of time-series InSAR technologies in mining subsidence, which improved the magnitude of InSAR deformation monitoring to some extent [22–25]. However, such methods must be based on a large amount of SAR images, and their improvement is limited. Therefore, researchers have been exploring the integration of InSAR technologies with other methods, such as GPS, LiDAR and multi-source SAR images, as well as different model simulation data [26,27]. Concurrently, researchers have turned their attention to SAR image intensity data, exploring the feasibility of using offset tracking techniques to obtain the deformation field of surface subsidence in mining areas [28,29]. However, offset tracking methods are limited by image spatial resolution and registration accuracy. Therefore, their application in mining subsidence monitoring is still not consistent.

Numerous studies have shown that the scale of the surface deformation detectable by InSAR is theoretically proportional to the wavelength of the SAR system. Sub-band InSAR, on the other hand, can simulate a longer wavelength, and thus, facilitates the analysis of large-scale surface deformations. This technique was first proposed by Madsen and Zebker and it derives from conventional InSAR [30]. To date, this technology has been successfully applied in the fields of seismic and co-seismic deformation field extractions, large artificial buildings, and deformation monitoring of copper mining areas [21–35]. However, few studies have focused on the applicability of this technology in deformation monitoring of coal mining subsidence areas.

Based on an in-depth analysis of the basic principles of sub-band InSAR, the present study confirmed the challenges of performing registration of master and slave images using conventional sub-band InSAR processing. Moreover, the geocoding of the differential interferometry was also difficult with conventional approaches, resulting in inaccuracies in the final deformation interpretation results. In this paper, we proposed a new method to

facilitate sub-band InSAR processing by using a registration offset file and a refined lookup table generated via full-bandwidth single-look complex (SLC) image interference.

2. Materials and Methods

2.1. Basic Principle of Sub-Band InSAR

The implementation of sub-band interferometry is based on the split-spectrum of SLC images in range direction. The so-called “sub-band” refers to a signal that decomposes the raw bandwidth signal into only part of the full-band in the frequency domain. These “sub-band” signals have the same information in the time domain (or spatial domain) as the raw signal, but only contain the frequency energy within the reserved bandwidth in the frequency domain. The split-spectrum of SLC images in range direction is often implemented with a band-pass filter. The basic principle and specific implementation process are as follows:

Through a band-pass filter, the full-band master and slave SLC images are divided into non-overlapping upper and lower sub-bands, respectively (Figure 1). In Figure 1, B is the full bandwidth of the SAR system, and b is the sub-band bandwidth.

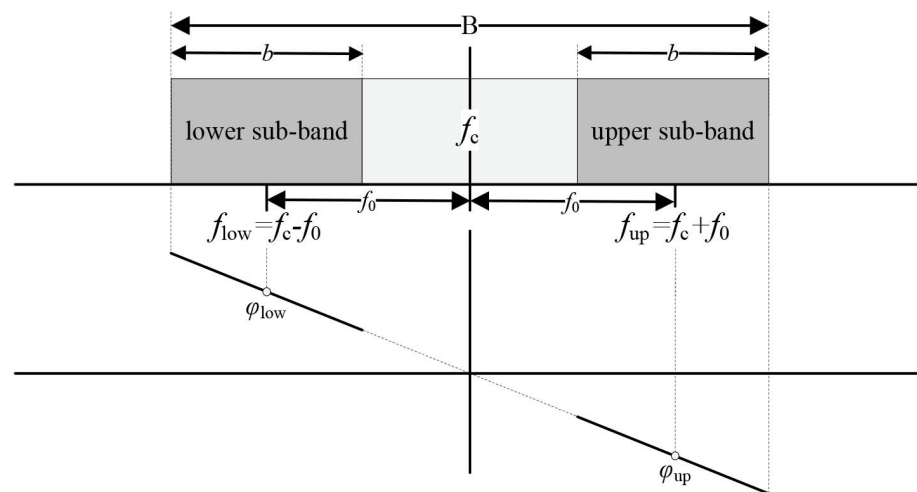


Figure 1. Schematic diagram of full bandwidth and sub-band split-spectrum of a SAR system.

Assuming that the radar carrier frequency and offset frequency are f_c (which can be obtained from the parameter file of SAR image) and f_0 , respectively, the central frequencies of upper and lower sub-bands after split-spectrum (f_{up} and f_{low}) can be expressed with the following equations:

$$\begin{cases} f_{low} = f_c - f_0 \\ f_{up} = f_c + f_0 \end{cases} \quad (1)$$

Performing the initial interferometric processing [36], the differential phase of the upper and lower sub-band image pairs (f_{up} and f_{low}) can be expressed as follows:

$$\begin{cases} \phi_{up} = 4\pi \frac{f_c + f_0}{c} \Delta r \\ \phi_{low} = 4\pi \frac{f_c - f_0}{c} \Delta r \end{cases} \quad (2)$$

where c is the speed of light and Δr is the slant differential range of the master and slave image.

Performing the second interferometric processing of the differential phase of different sub-bands, the final sub-band differential phase ϕ_{sub} can be obtained as follows:

$$\phi_{sub} = \phi_{up} - \phi_{low} = 4\pi \frac{2f_0}{c} \Delta r \quad (3)$$

Then, the ratio K of the sub-band InSAR-simulated wavelength γ_k to the raw radar system wavelength γ can be expressed as follows:

$$K = \frac{\gamma_k}{\gamma} = \frac{\phi}{\phi_{\text{sub}}} = \frac{f_c}{2f_0} \quad (4)$$

where ϕ represents the full-band differential interference phase.

As shown in Figure 1, the offset frequency f_0 ranges from 0 to $0.5B$, and for the current radar system, bandwidth B is much smaller than the centre frequency f_c . Therefore, the simulated wavelength can be increased by one or even two orders of magnitude through sub-band InSAR, and the deformation gradient will decrease accordingly, which may serve the purpose of large-scale deformation monitoring. The nomenclature of symbols and abbreviations is shown in Table 1.

Table 1. The nomenclature table of symbols.

Symbol	Description	Unit
f_c	Carrier frequency of radar	Hz
f_0	Offset frequency	Hz
f_{up}	Central frequencies of upper sub-bands	Hz
f_{low}	Central frequencies of lower sub-bands	Hz
ϕ_{up}	Differential phase of the upper sub-band image pairs	rad
ϕ_{low}	Differential phase of the lower sub-band image pairs	rad
c	Speed of light	m/s
Δr	Slant differential range of master and slave image	m
ϕ_{sub}	Differential phase of the final sub-band	rad
γ	Wavelength of raw radar system	mm
γ_k	Wavelength of sub-band InSAR-simulated	mm

2.2. Process of Deformation Extraction Based on Sub-Band InSAR

Sub-band InSAR is a derivative of conventional InSAR, and its deformation extraction process is similar to the conventional D-InSAR. In 2009, Bircic et al. analysed and summarised sub-band InSAR processing with TerraSAR-X data for absolute phase extraction [37], as shown in Figure 2.

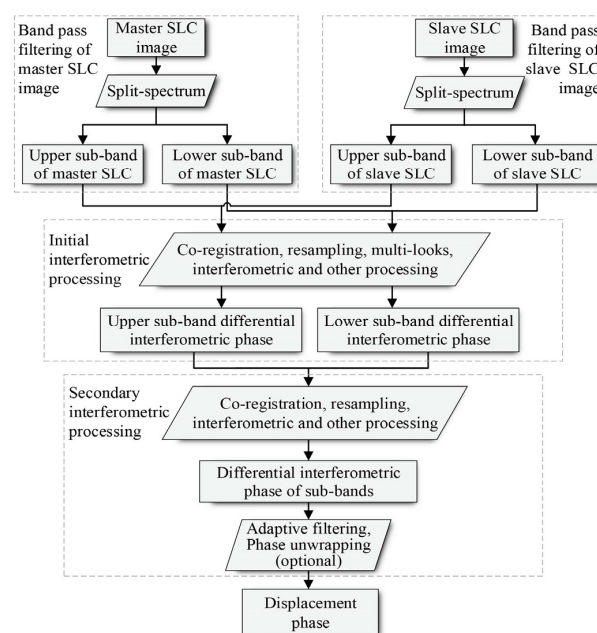


Figure 2. Flowchart of conventional sub-band InSAR.

The specific steps are the following: (1) Range split-spectrum of full-band master and slave SLC images is obtained through a band-pass filter, and an upper and lower sub-band SLC pair is generated. (2) Registration, resampling, initial interferometry and other processing are performed between sub-bands of master and slave SLC images, and upper and lower sub-band interferograms are generated. (3) Registration, resampling, second interferometry and other processing are performed between the upper and lower sub-band phase, and a final sub-band interferometric phase is generated. (4) Adaptive filtering and phase unwrapping are performed and a displacement phase is generated.

2.3. Improvement of Sub-Band InSAR Processing

Among the previously mentioned InSAR processing methods, the range split-spectrum method [38] is applied before registration and resampling, which results in three main drawbacks: (1) The resolution of sub-band SAR images is reduced, which increases the difficulty of registration between sub-band images and the error of the first interferometric phase. (2) Inconsistencies occur between the registration offset polynomials of upper and lower sub-band image pairs, which leads to errors in the second interferometry, and linear stripes may appear in the interferogram due to the Doppler centroid shift. (3) The geocoding for differential interferogram is challenging due to the loss of resolution.

Ideally, the offset polynomials of upper and lower sub-band image pairs should be the same as the offset polynomials between the full-band master and slave images. Additionally, there should be no offset between the upper and lower sub-band interferometric phase. Therefore, based on these premises, the registration of upper and lower sub-band image pairs can be performed utilising the offset information between the full-band master and slave images. This not only effectively reduces the registration error due to resolution loss but also avoids the appearance of linear stripes, characteristic of the conventional sub-band InSAR processing caused by the Doppler centroid shift. To overcome the difficulty of achieving accurate geocoding caused by sub-band decomposition, we innovatively propose the idea of using a refined lookup table obtained by accurately matching the original high-resolution intensity image and digital elevation model (DEM) to facilitate sub-band interference geocoding.

The improved sub-band InSAR processing flow diagram is presented in Figure 3. The specific steps are outlined below:

- (1) Registration of raw SLC images: The full-band master and slave images are registered using an intensity cross-correlation approach to obtain registration offset data.
- (2) Range split-spectrum: Through a band-pass filter, the full-band master and slave SLC images are divided into non-overlapping upper and lower sub-bands, respectively.
- (3) Registration, resampling, initial interferometric, and filtering of sub-band pairs: Completion of the registration and resampling between upper and lower sub-band image pairs by using the registration offset information obtained in the first step. The initial interferometric of sub-band pairs and filtering of sub-band phase are also performed separately.
- (4) Removal of the topography phase: Utilization of an external DEM and the multi-looks intensity data of the raw SLC image to generate a refined lookup table, followed by the removal of the topography phase from the upper and lower sub-band interferometric phases, respectively.
- (5) Fusion of the sub-band interferometric phase: The second interferometric processing of sub-band phase obtained in the previous step is employed to obtain a sub-band interferogram. In this process, the simulated radar wavelength is effectively expanded, and the noise is also amplified accordingly; the signal-to-noise ratio is often low.
- (6) Removal of residual phase trends and phase unwrapping.
- (7) Geocoding: Due to the sub-band decomposition, the resolution of the SLC image is reduced. Therefore, the sub-band interference geocoding process needs to be completed by means of the refined lookup table obtained by the accurate matching of the original high-resolution intensity image and DEM in Step 4.

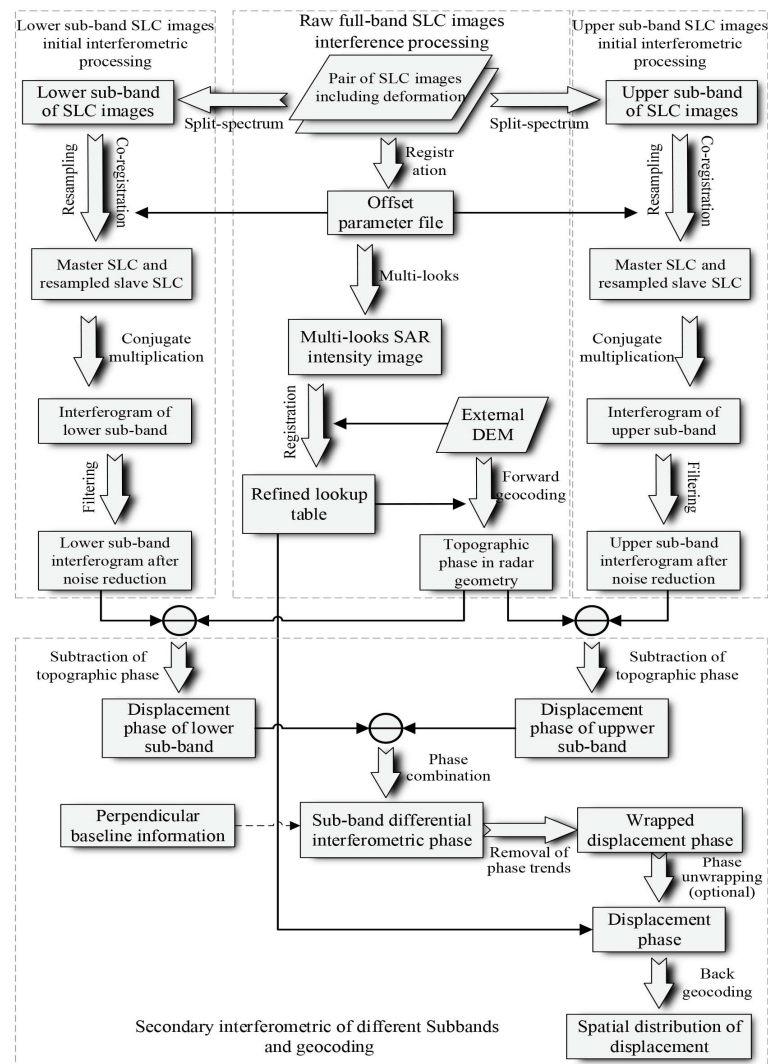


Figure 3. Ground surface deformation extraction process of sub-band InSAR.

3. Experiments

3.1. Noiseless Simulation Experiments

3.1.1. Simulation of Surface Deformation Data and Wrapped Phase

The red line in Figure 4 represents an actual underground mining working face. The location, mining size, and mining depth of the working face are also indicated in Figure 4.

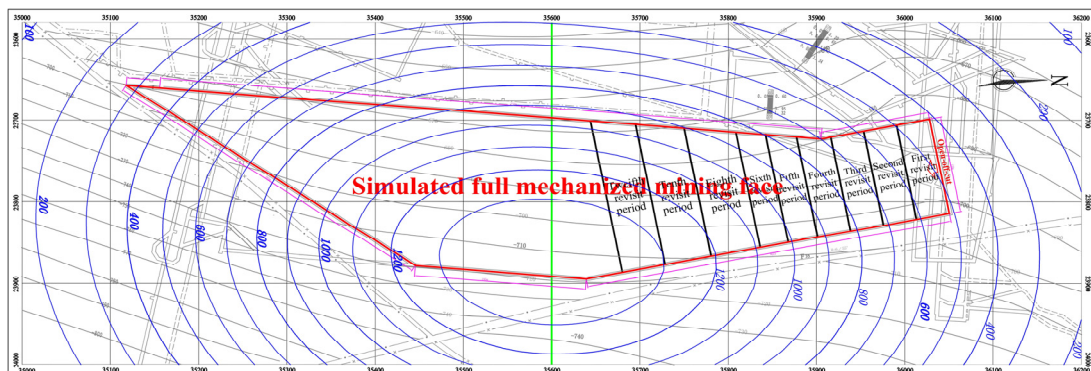


Figure 4. Simulated mining working face and predicted surface subsidence contours.

Usually, surface subsidence and deformation can be calculated when the underground mining area and geological mining conditions are determined using the corresponding method. The probability integral method, proposed by Litwiniszyn [39] and generalised by Liu and Liao [40], is one of the most widely used and most well-developed methods. In this section, the probability integration model was used to predict the surface subsidence caused by the mining of this working face (predicted parameters are summarised in Table 2), and the predicted deformation is then taken as the true surface deformation information (the blue curves in Figure 4 represent the surface subsidence contour).

Table 2. Prediction parameters of the probability integral method.

Parameters	Value	Parameters	Value
Subsidence factor	0.78	Displacement factor	0.3
Tangent of major influence angle	1.70	Greatest subsidence angle (deg)	84
Deviation of inflection point (m)	0	Mining coal thickness (m)	5.80

Figure 5a,b show the true phase and wrapped phase of the simulated surface deformation, respectively, which were simulated based on the TerraSAR-X satellite parameters (Table 3). The reason for choosing TerraSAR-X satellite parameters for the simulation is that this satellite has a longer bandwidth than C-band and L-band satellites.

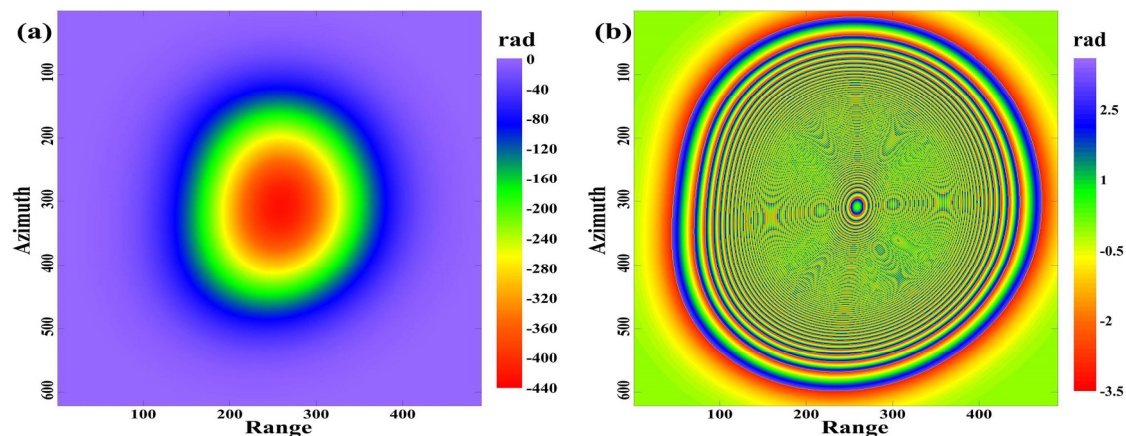


Figure 5. True phase and wrapped phase of the simulated surface deformation: (a) true phase; and (b) wrapped phase.

Table 3. Simulated parameters of the TerraSAR-X satellite.

Parameters	Value	Parameters	Value
Wavelength (mm)	31	Bandwidth (MHz)	100
Incident angle (deg)	41.07	Resolution (m) (Range \times Azimuth)	3×3
Frequency (GHz)	9.65		

Figure 5 shows that the true phase of the simulated surface deformation reaches 440 rad, and it includes nearly seventy whole-cycle phase transitions (which exceeds the largest detectable deformation variable of the conventional D-InSAR method). The interference fringes at the edge of the subsidence basin are clearly visible, and the stripe density near the centre of the basin gradually increases until the fringes become blurred and indistinguishable. This phenomenon increases the difficulty of phase unwrapping and leads to failures and errors in the unwrapping results, thus leading to inaccuracies in the extracted deformation.

3.1.2. Sub-Band Decomposition and Interference

Based on the basic principles of the aforementioned sub-band interference, if the sub-band bandwidth is set to $0.2B$, the offset of the sub-band centre frequency should be $0.4B$ (i.e., 40 MHz), then the centre frequencies of the upper and lower sub-bands are, respectively 9.69 GHz and 9.61 GHz. Figure 6 illustrates the interferometric phase of upper and lower sub-bands with different centre frequency (Figure 6a and 6b, respectively), the final sub-band phase after the second interferometric processing is also shown (Figure 6c).

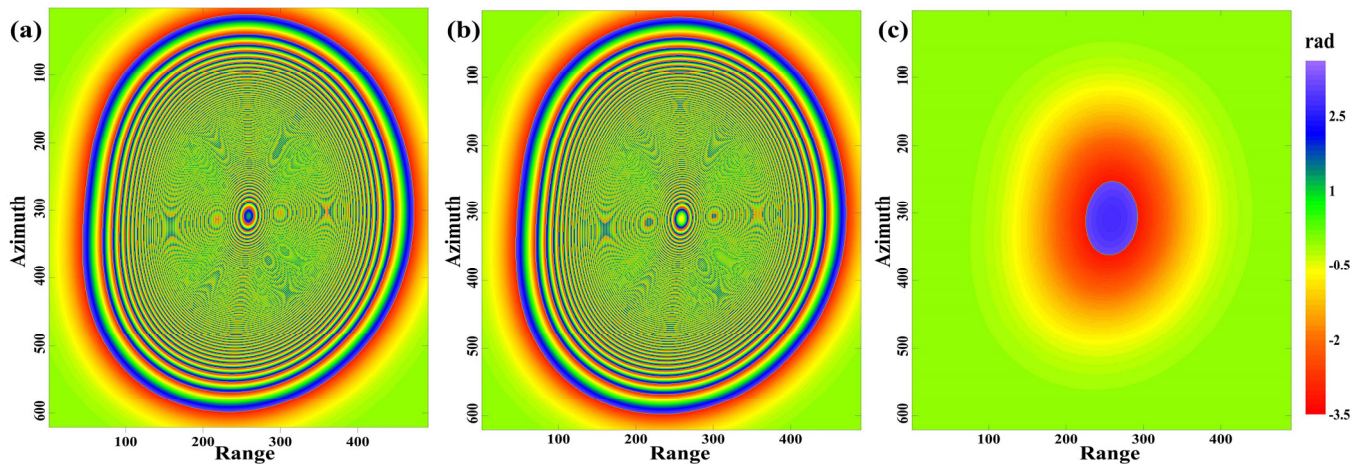


Figure 6. Wrapped phase of sub-band InSAR: (a) upper sub-band interferometric phase; (b) lower sub-band interferometric phase; and (c) final sub-band interferometric phase.

Figure 6a,b show that although the centre frequencies of the upper and lower sub-bands are different, the interferometric phase of each sub-band is not significantly different from the original interferometric phase due to the small offset amplitude, thus, the stripe density is still very high. Figure 6c illustrates the sub-band interferometric phase with a central frequency of 0.08 GHz, corresponding to a simulated wavelength of about 3.74 m causing the number of fringes in the interferogram to decrease significantly and exhibit only one whole-cycle phase transition. The difference of the centre frequencies of the upper and lower sub-bands makes the interferometric phases of the respective simulated deformations slightly different. This slight phase difference reduces the fringe density in the sub-band interferogram when the second interferometric processing is performed.

3.1.3. Accuracy Analysis

To analyse and evaluate the accuracy of the surface deformation obtained by the sub-band InSAR method, the final sub-band phase in Figure 6c was converted to a surface deformation value and the position with a north coordinate of 35,600 (indicated by the green line in Figure 4) was selected to generate the subsidence curve. The surface deformation monitoring results of the sub-band InSAR method are compared with the true subsidence in Figure 7.

The comparison in Figure 7 shows that the sub-band InSAR-monitored results can accurately depict the actual surface deformations and exhibit good consistency in the spatial distribution and deformation values. Statistical analysis shows that the average and maximum difference between the sub-band InSAR-monitored results and real surface deformations are 9 mm and 26 mm, respectively, and the proportion of maximum vertical deformation (1397 mm) is roughly 0.64% and 1.86%, respectively. The experimental results show that the deformation monitoring accuracy of sub-band InSAR can reach centimetre level under noiseless conditions, which fully meets the requirements of mining subsidence monitoring.

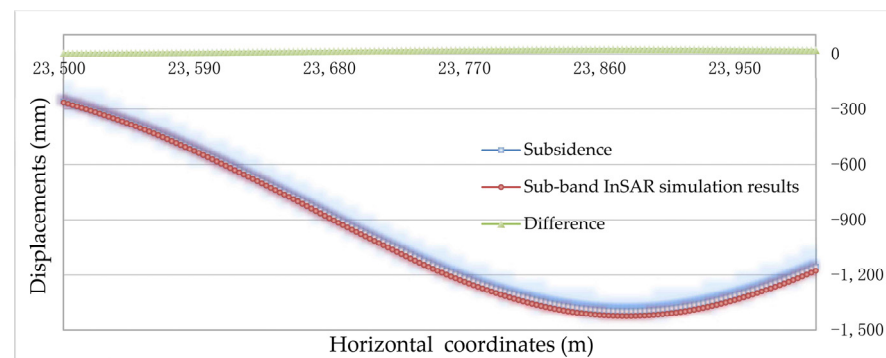


Figure 7. Comparison of ground surface deformation monitoring results with sub-band InSAR and true vertical displacements.

3.2. Monitoring and Analysis of Surface Dynamic Deformation in Mining Subsidence Areas

The simulation experiment under noiseless conditions in Section 3.1 shows that the sub-band InSAR processing method can effectively reduce the fringe density in the interferogram and the difficulty of phase unwrapping. This, in turn, facilitates monitoring for large-scale surface deformation caused by the full mining of the working face. However, the full depletion of a mining working face is not accomplished overnight; rather, surface subsidence represents a gradual and dynamic evolution process. This section will focus on the applicability of sub-band InSAR for surface deformation monitoring in the working face mining process.

3.2.1. Dynamic Deformation Simulation Caused by Working Face Mining

The analyses henceforth described will continue to be based on the working face simulated in Section 3.1. The average mining thickness of the working face is assumed to be 5.8 m, and the daily coal output is 2400 tonnes. The approximate mining area throughout the different revisit cycles (11 days per cycle) of TerraSAR-X are indicated in Figure 4 with black lines. Figure 8 shows the calculated surface deformation caused by the mining of the corresponding working face for each different SAR satellite revisit period. This was calculated by the probability integral method, based on the prediction parameters summarised in Table 2.

Figure 8a–i shows the spatial distribution of surface subsidence caused by underground working face mining in the SAR satellite’s 1st, 2nd, 3rd, 4th, 5th, 6th, 8th, 10th, and 12th revisit cycles. The statistics of the maximum surface subsidence value in each different revisit period are summarized in Table 4.

Table 4. Prediction parameters of the probability integral method.

Revisit Period	Maximum Subsidence (mm)	Revisit Period	Maximum Subsidence (mm)
1st	88	6th	520
2nd	178	8th	647
3rd	264	10th	782
4th	355	12th	906
5th	431		

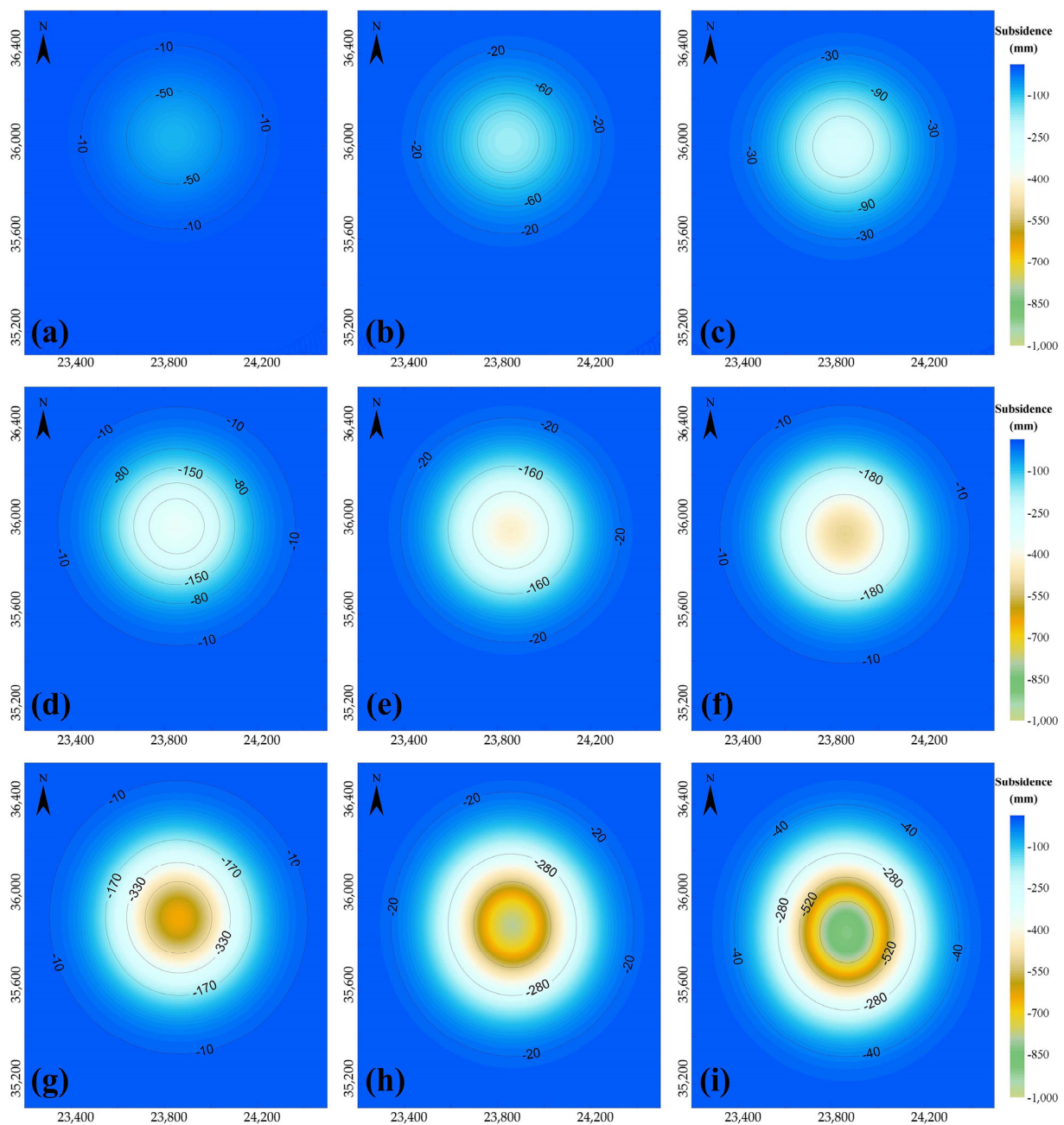


Figure 8. Surface deformation corresponding to different SAR satellite revisit periods: (a) 1st revisit cycle; (b) 2nd revisit cycle; (c) 3rd revisit cycle; (d) 4th revisit cycle; (e) 5th revisit cycle; (f) 6th revisit cycle; (g) 8th revisit cycle; (h) 10th revisit cycle; and (i) 12th revisit cycle.

3.2.2. Wrapped Phase with Noise

According to the SAR satellite parameters in Table 3, the predicted surface deformation was phase-transformed after which the deformation phase was wrapped, then the differential interferometric phase of surface deformation monitored by the TerraSAR-X satellite was simulated. To explore the influence of noise, this section incorporates random noise between in the interferogram, as shown in Figure 9.

The interferogram simulated in Figure 9 shows that with increasing SAR image time intervals, which correspond to increasing surface subsidence, the number and density of interference fringes increase as well. In the 2nd revisit period of the TerraSAR-X satellite (corresponding to a maximum surface deformation of 178 mm), interference fringes are evident in the interferograms. After the first two revisit periods (Figure 9c), the interference

fringes become blurred due to increasing surface subsidence and noise. Additionally, significant discontinuities have occurred between the pixels. In particular, starting from the 4th revisit period, as depicted in Figure 9d, the noise speckles have made the interference fringes indistinguishable. In these conditions, conventional D-InSAR is not well-suited for surface deformation monitoring.

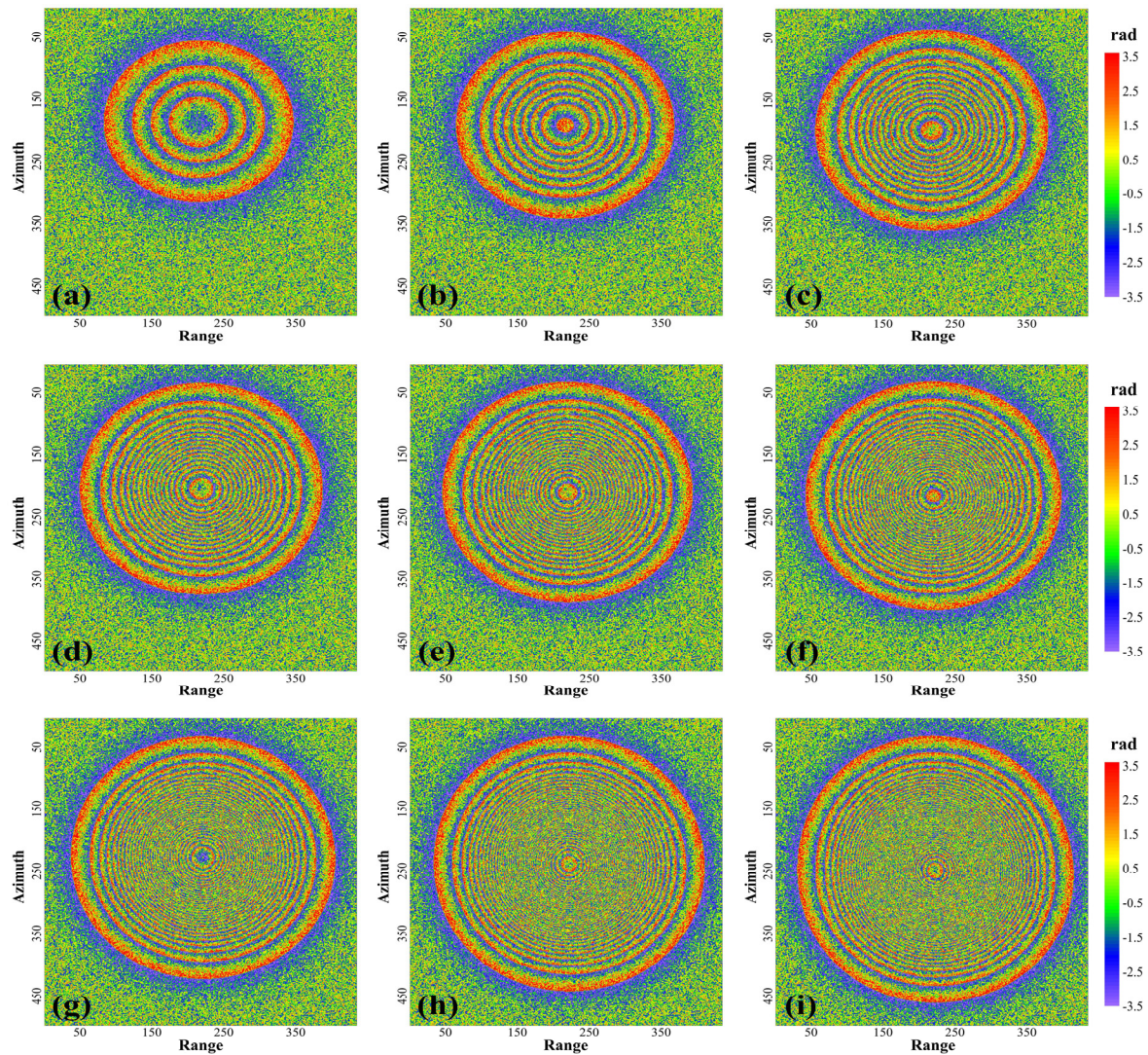


Figure 9. Wrapped D-InSAR phase of a noisy surface deformation: (a) 1st revisit cycle; (b) 2nd revisit cycle; (c) 3rd revisit cycle; (d) 4th revisit cycle; (e) 5th revisit cycle; (f) 6th revisit cycle; (g) 8th revisit cycle; (h) 10th revisit cycle; and (i) 12th revisit cycle.

3.2.3. Sub-Band Interferometric Phase

According to the parameters of the TerraSAR-X satellite (Table 3) and assuming a sub-band bandwidth and centre frequency offset of $0.2B$ and 40 MHz, respectively, we simulated the sub-band interferometric phase in the dynamic mining process of the aforementioned working surface (Figure 10).

A comparison of the D-InSAR interferometric phase in Figure 9 with the sub-band interferometric phase in Figure 10, clearly shows that sub-band InSAR processing considerably reduces the interference fringe density. However, due to a simulated wavelength increase of one to even two orders of magnitude, there is a sharp decrease in the interferometric phase, resulting in significant noise impact. Difficulty in distinguishing the noise from the sub-band interferometric phase occurs, especially in surface areas with relatively small deformations. Figure 10a–c illustrate that the sub-band interferometric phases of the surface deformation

(264 mm) occurring during the first three revisit periods of TerraSAR-X satellite are completely obscured by noise. Starting from the 4th revisit period, the interferometric phase gradually appears, and from the 8th revisit period onwards (corresponding to a maximum surface subsidence 647 mm), the deformation interferometric phase becomes clear.

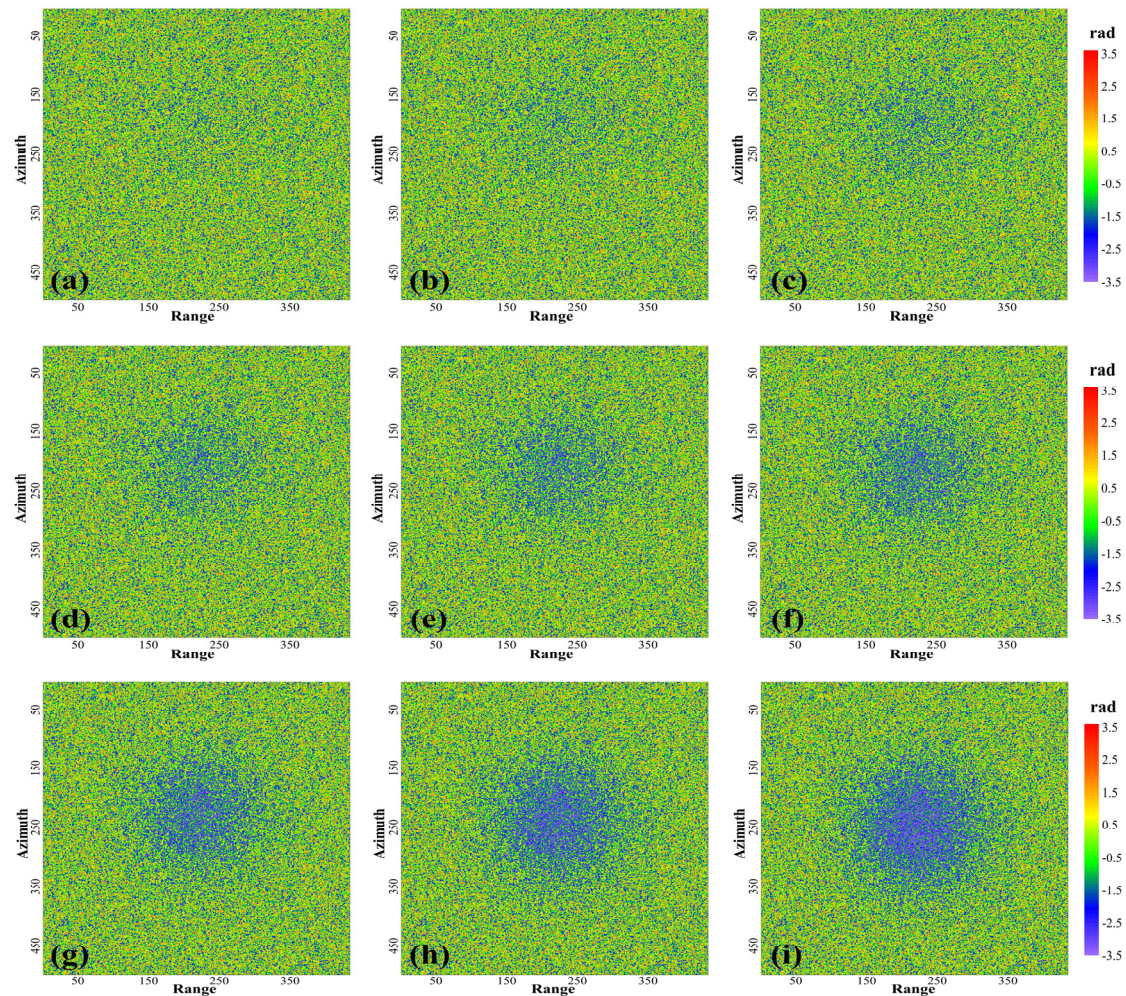


Figure 10. Simulated wrapped phase of sub-band InSAR: (a) 1st revisit cycle; (b) 2nd revisit cycle; (c) 3rd revisit cycle; (d) 4th revisit cycle; (e) 5th revisit cycle; (f) 6th revisit cycle; (g) 8th revisit cycle; (h) 10th revisit cycle; and (i) 12th revisit cycle.

3.2.4. Applicability Analysis of Sub-Band InSAR

A comparison of Figure 9a,b with Figure 10a,b, reveals that in surface subsidence areas with small-scale deformation, the conventional D-InSAR method can effectively serve the purposes of deformation monitoring, while the interferometric phase obtained by the sub-band InSAR is completely overwhelmed by noise. The results show that the sub-band InSAR method cannot be applied to extract small-scale deformations.

A further comparison Figure 9c–f with Figure 10c–f, shows that with increased surface subsidence, the conventional D-InSAR method is gradually unable to monitor the deformation. Similarly, the sub-band interferometric phases are barely apparent and evidently affected by noise. This demonstrates that, given the bandwidth range of current SAR satellites, relying only on conventional D-InSAR and sub-band InSAR approaches is still insufficient to achieve complete monitoring of surface deformation caused by underground coal mining, as this results in substantial “blind spots” for certain deformation monitoring intervals.

Moreover, Figures 9g–i and 10g–i illustrate that the conventional D-InSAR method fails as surface subsidence increases, despite the method being effective for the deformation

extraction of subsidence boundary areas with small deformations. At this point, the interferometric phase obtained by sub-band InSAR becomes clear, and its advantages gradually become apparent. In these instances, sub-band interferometry is superior to conventional D-InSAR for large-scale surface deformation monitoring. However, it does not necessarily mean that it can effectively serve the purpose of deformation monitoring since large-scale surface deformation often leads to low coherence of the study area, and coherence is the basis of interferometry.

In summary, the sub-band InSAR method may not be well-suited to monitor mining subsidence, unless the surface deformation caused by underground mining forms marked sub-band interference fringes. The formation of these interference fringes depends not only on the coherence of the region but mainly on the offset of the centre frequency in the sub-band InSAR process, which in turn is limited by the bandwidth of the raw SLC image.

Presently, the maximum image bandwidth of SAR systems in orbit is 300 MHz; therefore, the maximum offset of a sub-band centre is only 0.15 GHz, accounting for a small proportion of the 9.65 GHz of the original image centre frequency. This makes it very difficult for sub-band InSAR to form clear interference fringes. Therefore, the applicability of sub-band InSAR for mining subsidence monitoring will depend on both the surface deformation and coherence of a given region of interest.

4. Discussion and Conclusions

In the present study, the sub-band InSAR method effectively increased the simulated wavelength, reduced the number of interference fringes, as well as the difficulty of phase unwrapping, facilitating the applicability of large-scale surface deformation extraction. Simulation experiments under noiseless conditions provided evidence that the improved sub-band InSAR processing method could be theoretically applied to the monitoring of surface subsidence caused by full mining of the working face.

The simulated experimental results show that the maximum difference between the sub-band InSAR-monitored results and real surface deformations is 26 mm (the proportion of maximum vertical deformation is roughly 1.86%) under noiseless conditions, which fully meets the requirements of mining subsidence monitoring.

Dynamic deformation monitoring simulations with random noise showed that the sub-band interferometric phase gradually appears when the surface deformation reaches one-tenth of the simulated wavelength. When the deformation reaches one-fifth of the simulated wavelength, the interferometric phase becomes clear, demonstrating the advantage of the sub-band InSAR method in these conditions. Moreover, it is widely accepted that when the deformation is lower than one-quarter of the simulated wavelength, the phase unwrapping operation can be omitted. However, due to the limitation of the SAR system bandwidth, the radar wavelength simulated by the sub-band InSAR could not be optimised to the surface deformation, and often reached tens or even hundreds of times the raw wavelength. These drawbacks led to difficulties in the formation of interference fringes in the monitoring of dynamic mining subsidence, and the interferometric phase was significantly affected by noise. Therefore, the image bandwidth of current SAR satellite sensors becomes the most important factor limiting the application of sub-band InSAR in deformation monitoring. Moreover, in order to form a distinct deformation interferometric phase in the sub-band interferogram, it is often necessary to increase the imaged time interval between the master and slave images to mask the influence of noise. This causes the coherence between images to drop sharply, and noise is further introduced, which limits the formation of interference fringes.

In summary, it is difficult to apply sub-band InSAR to the dynamic monitoring of mining subsidence with current SAR images; this is mainly due to limited image bandwidth and site coherence. However, the experimental results of simulated dynamic deformation monitoring show that for high-coherence regions where surface deformation exceeds $1/5$ to $1/4$ of the simulated wavelength in a short time, the sub-band InSAR method may

be useful. Moreover, its deformation monitoring accuracy could theoretically meet the needs of mining subsidence monitoring, according to our observations.

Focusing on the shortcomings of the current methods in sub-band InSAR processing, this study proposed an improved processing workflow and conducted a preliminary investigation on the applicability of sub-band InSAR technologies in coal mining subsidence monitoring. For coherence, we can focus the research objects from the area to individual high-coherence points. In future studies, the integration of sub-band interference with other measurement modes or data should be explored to achieve an optimised mining subsidence monitoring strategy.

Author Contributions: Conceptualization, X.D. and K.W.; methodology, X.D.; software, Q.S. and K.W.; validation, Q.S., J.Y. and X.L.; formal analysis, Q.S.; investigation, X.D.; resources, Q.S.; data curation, Q.S.; writing—original draft preparation, X.D.; writing—review and editing, Q.S.; visualization, J.Y.; supervision, K.W.; project administration, X.D.; funding acquisition, X.D. All authors have read and agreed to the published version of the manuscript.

Funding: This work was supported by the National Natural Science Foundation of China [grant number 52104174], by the Natural Science Foundation of Jiangsu Province [grant number BK20190642], and the Major Research Plan of the Ningxia Hui Autonomous Region [grant number 2022BEG03065].

Institutional Review Board Statement: Not applicable.

Informed Consent Statement: Not applicable.

Data Availability Statement: Not applicable.

Acknowledgments: The authors are grateful to the anonymous reviewers for their valuable suggestions.

Conflicts of Interest: The authors declare no conflict of interest.

References

1. Carotenuto, A.; Ceglia, F.; Marrasso, E.; Sasso, M.; Vanoli, L. Exergoeconomic optimization of polymeric heat exchangers for geothermal direct applications. *Energies* **2021**, *14*, 6994. [CrossRef]
2. Ceglia, F.; Marrasso, E.; Roselli, C.; Sasso, M. Time-evolution and forecasting of environmental and energy performance of electricity production system at national and at bidding zone level. *Energy Convers. Manag.* **2022**, *265*, 115772. [CrossRef]
3. BP Statistical Review of World Energy 2022. Available online: <https://www.bp.com/content/dam/bp/business-sites/en/global/corporate/pdfs/energy-economics/statistical-review/bp-stats-review-2022-full-report.pdf> (accessed on 28 June 2022).
4. Diao, X.; Bai, Z.; Wu, K.; Zhou, D.; Li, Z. Assessment of mining-induced damage to structures using InSAR time series analysis: A case study of Jiulong Mine, China. *Environ. Earth Sci.* **2018**, *77*, 166. [CrossRef]
5. Diao, X.; Wu, K.; Zhou, D.; Wang, J.; Duan, Z.; Yu, Z. Combining subsidence theory and slope stability analysis method for building damage assessment in mountainous mining subsidence regions. *PLoS ONE* **2019**, *14*, 2100212. [CrossRef] [PubMed]
6. Diao, X.; Wu, K.; Zhou, D.; Li, L. Integrating the probability integral method for subsidence prediction and differential synthetic aperture radar interferometry for monitoring mining subsidence in Fengfeng, China. *J. Appl. Remote Sens.* **2016**, *10*, 016028. [CrossRef]
7. Carboni, F.; Porreca, M.; Valerio, E.; Mariarosaria, M.; Luca, C.D.; Azzaro, S.; Ercoli, M.; Barchi, M.R. Surface ruptures and off-fault deformation of the October 2016 central Italy earthquakes from DInSAR data. *Sci Rep.* **2022**, *12*, 3172. [CrossRef] [PubMed]
8. Tiwari, A.; Dwivedi, R.; Dikshit, O.; Singh, A. A study on measuring surface deformation of the L'Aquila region using the StaMPS technique. *Int. J. Remote Sens.* **2016**, *37*, 819–830. [CrossRef]
9. Huang, Z.; Zhang, G.; Shan, X.; Gong, W.; Zhang, Y.; Li, Y. Co-Seismic Deformation and Fault Slip Model of the 2017 Mw 7.3 Darbandikhan, Iran-Iraq Earthquake Inferred from D-InSAR Measurements. *Remote Sens.* **2019**, *11*, 2521. [CrossRef]
10. Tung, H.; Chen, H.Y.; Hsu, Y.J.; Hu, J.C.; Chang, Y.H.; Kuo, Y.T. Triggered slip on multifaults after the 2018 Mw 6.4 Hualien earthquake by continuous GPS and InSAR measurements. *Terr. Atmos. Ocean. Sci.* **2019**, *30*, 285–300. [CrossRef]
11. Jo, M.; Jung, H.; Won, J.; Lundgren, P. Measurement of three-dimensional surface deformation by Cosmo-SkyMed X-band radar interferometry: Application to the March 2011 Kamoamo fissure eruption, Kilauea volcano, Hawaii. *Remote Sens. Environ.* **2015**, *169*, 176–191. [CrossRef]
12. Patrick, M.R.; Dehn, J.; Papp, K.R.; Lu, Z.; Dean, K.; Moxey, K.; Izbekov, P.; Guritz, R. The 1997 eruption of Okmok volcano, Alaska: A synthesis of remotely sensed imagery. *J. Volcanol. Geotherm. Res.* **2003**, *127*, 87–105. [CrossRef]
13. Talledo, D.A.; Miano, A.; Bonano, M.; Di Carlo, F.; Lanari, R.; Manunta, M.; Meda, A.; Mele, A.; Prota, A.; Saetta, A.; et al. Satellite radar interferometry: Potential and limitations for structural assessment and monitoring. *J. Build. Eng.* **2022**, *46*, 103756. [CrossRef]
14. Mele, A.; Miano, A.; Di Martire, D.; Infante, D.; Ramondini, M.; Prota, A. Potential of remote sensing data to support the seismic safety assessment of reinforced concrete buildings affected by slow-moving landslides. *Arch. Civ. Mech. Engineering.* **2022**, *22*, 88. [CrossRef]

15. Chen, C.; Zhu, K.; Xu, P.; Shan, B.; Yang, G.; Song, S. Refined landslide susceptibility analysis based on InSAR technology and UAV multi-source data. *J. Clean. Prod.* **2022**, *368*, 133146.
16. Strozzi, T.; Caduff, R.; Jones, N.; Barboux, C.; Delaloye, R.; Bodin, X.; Käab, A.; Mätzler, E.; Schrott, L. Monitoring Rock Glacier Kinematics with Satellite Synthetic Aperture Radar. *Remote Sens.* **2020**, *12*, 559. [[CrossRef](#)]
17. Auriac, A.; Sigmundsson, F.; Hooper, A.; Spaans, K.H.; Bjornsson, H.; Palsson, F.; Pinel, V.; Feigl, K.L. InSAR observations and models of crustal deformation due to a glacial surge in Iceland. *Geophys. J. Int.* **2014**, *198*, 1329–1341. [[CrossRef](#)]
18. Kumar, V.; Venkataraman, G.; Høgda, K.A.; Larsen, Y. Estimation and validation of glacier surface motion in the northwestern Himalayas using high-resolution SAR intensity tracking. *Int. J. Remote Sens.* **2013**, *34*, 5518–5529. [[CrossRef](#)]
19. Przyłucka, M.; Herrera, G.; Graniczny, M.; Colombo, D.; Béjar-Pizarro, M. Combination of conventional and advanced DInSAR to monitor very fast mining subsidence with TerraSAR-X Data: Bytom City (Poland). *Remote Sens.* **2015**, *7*, 5300–5328. [[CrossRef](#)]
20. Zhang, Z.; Wang, C.; Tang, Y.; Zhang, H.; Fu, Q. Analysis of ground subsidence at a coal-mining area in Huainan using time-series InSAR. *Int. J. Remote Sens.* **2015**, *36*, 5790–5810. [[CrossRef](#)]
21. Samsonov, S.; d’Oreye, N.; Smets, B. Ground deformation associated with post-mining activity at the French–German border revealed by novel InSAR time series method. *Int. J. Appl. Earth Obs.* **2013**, *23*, 142–154. [[CrossRef](#)]
22. Wang, L.; Deng, K.; Fan, H.; Zhou, F. Monitoring of large-scale deformation in mining areas using sub-band InSAR and the probability integral fusion method. *Int. J. Remote Sens.* **2018**, *40*, 2602–2622. [[CrossRef](#)]
23. Fan, H.; Lu, L.; Yao, Y. Method Combining Probability Integration Model and a Small Baseline Subset for Time Series Monitoring of Mining Subsidence. *Remote Sens.* **2018**, *10*, 1444. [[CrossRef](#)]
24. Pawluszek-Filipiak, K.; Borkowski, A. Integration of DInSAR and SBAS Techniques to Determine Mining-Related Deformations Using Sentinel-1 Data: The Case Study of Rydułtowy Mine in Poland. *Remote Sens.* **2020**, *12*, 242. [[CrossRef](#)]
25. Bateson, L.; Cigna, F.; Boon, D.; Sowter, A. The application of the Intermittent SBAS (ISBAS) InSAR method to the South Wales Coalfield, UK. *Int. J. Appl. Earth Obs.* **2014**, *34*, 249–257. [[CrossRef](#)]
26. Ng, A.H.; Ge, L.; Du, Z.; Wang, S.; Ma, C. Satellite radar interferometry for monitoring subsidence induced by longwall mining activity using Radarsat-2, Sentinel-1 and ALOS-2 data. *Int. J. Appl. Earth Obs.* **2017**, *61*, 92–103. [[CrossRef](#)]
27. Chatterjee, R.S.; Thapa, S.; Singh, K.B.; Varunakumar, G.; Raju, E.V.R. Detecting, mapping and monitoring of land subsidence in Jharia Coalfield, Jharkhand, India by spaceborne differential interferometric SAR, GPS and precision levelling techniques. *J. Earth Syst. Sci.* **2015**, *124*, 1359–1376. [[CrossRef](#)]
28. Huang, J.; Deng, K.; Fan, H.; Lei, S.; Yan, S.; Wang, L. An Improved Adaptive Template Size Pixel-Tracking Method for Monitoring Large-Gradient Mining Subsidence. *J. Sens.* **2017**, *2017*, 3059195. [[CrossRef](#)]
29. Chen, B.; Deng, K.; Fan, H.; Yu, Y. Combining SAR interferometric phase and intensity information for monitoring of large gradient deformation in coal mining area. *Eur. J. Remote Sens.* **2015**, *48*, 701–717. [[CrossRef](#)]
30. Madsen, S.N.; Zebker, H.A. Automated Absolute Phase Retrieval in Across-Track Interferometry. *Proc. Geosci. Remote Sens. Symp.* **1992**, *2*, 1582–1584.
31. Yu, L.; Shan, X.; Song, X.; Qu, C. Deformation of the 2013 Pakistan Mw 7.7 earthquake derived from sub-band InSAR. *Chinese J. Geophys.* **2016**, *59*, 1371–1382.
32. Tong, X.; Xu, X.; Chen, S. Coseismic Slip Model of the 2021 Maduo Earthquake, China from Sentinel-1 InSAR Observation. *Remote Sens.* **2022**, *14*, 436. [[CrossRef](#)]
33. Yang, D.; Qiu, H.; Ma, S.; Liu, Z.; Du, C.; Zhu, Y.; Cao, M. Slow surface subsidence and its impact on shallow loess landslides in a coal mining area. *Catena* **2022**, *209*, 105830. [[CrossRef](#)]
34. Vasile, G.; Boldo, D.; Boudon, R.; D’Urso, G.; Muja, R. Potential of Multipass Very High Resolution SAR Interferometry for Dam Monitoring. In Proceedings of the 9th Communications International Conference, Bucharest, Romania, 21–23 June 2012.
35. Wang, L.; Deng, K.; Zheng, M. Research on ground deformation monitoring method in mining areas using the probability integral model fusion D-InSAR, sub-band InSAR and offset-tracking. *Int. J. Appl. Earth Obs.* **2020**, *85*, 101981. [[CrossRef](#)]
36. Massonnet, D.; Rossi, M.; Carmona, C.; Adragna, F.; Peltzer, G.; Feigl, K.; Rabaute, T. The Displacement Field of the Landers Earthquake Mapped by Radar Interferometry. *Nature* **1993**, *364*, 138–142.
37. Brcic, R.E.; Bamler, R.M. Interferometric absolute phase determination with TerraSAR-X wideband SAR data. In Proceedings of the 2009 IEEE Radar Conference, Pasadena, CA, USA, 4–8 May 2009.
38. Fattahi, H.; Simons, M.; Agram, P. InSAR Time-Series Estimation of the Ionospheric Phase Delay: An Extension of the Split Range-Spectrum Technique. *IEEE Trans. Geosci. Remote* **2017**, *55*, 5984–5996. [[CrossRef](#)]
39. Litwiniyszyn, J. The theories and model research of movements of ground masses. In Proceedings of the European Congress on Ground Movement, Leeds, UK, 9–12 April 1957.
40. Liu, B.; Liao, G. *General Regulations of Ground Surface Movement in Coal Mine*; China Industry Press: Beijing, China, 1991.

Disclaimer/Publisher’s Note: The statements, opinions and data contained in all publications are solely those of the individual author(s) and contributor(s) and not of MDPI and/or the editor(s). MDPI and/or the editor(s) disclaim responsibility for any injury to people or property resulting from any ideas, methods, instructions or products referred to in the content.